

Chapter 2

Momentum Space Design of High- Q Photonic Crystal Microcavities

2.1 Introduction

As I have discussed in the preface, there has been a considerable amount of interest in extending cavity QED experiments to the semiconductor regime. In these experiments, coherent interactions between a single quantum dot (QD) and a single photon within the semiconductor microcavity can take place if the system is in the so-called strong coupling regime [9], where the QD-cavity coupling strength g exceeds the QD dephasing rate γ_{\perp} and the cavity decay rate κ . As of just a few years ago (i.e, at the start of our work in the area), no semiconductor microcavity had been demonstrated that had the requisite combination of a high quality factor (Q) and small mode volume (V_{eff}) to achieve strong coupling ($\kappa \sim 1/Q$, $g \sim 1/V_{\text{eff}}^{1/2}$). Photonic crystal (PC) microcavities seemed to be a particularly appealing route to semiconductor-based strong coupling; the ultrasmall volumes to which they confined light (smaller than the modal confinement that had been achieved in micropost or microdisk cavities, for example) implied that the Q values needed to achieve strong coupling would be more modest than in other geometries. The focus of this chapter is on the design of PC microcavities with sufficiently high Q s for these applications. It is based largely on references [21] and [23], which were published in July 2002 and March 2003.

While the PC microcavities studied in ref. [8] had very small mode volumes and loss properties sufficient to sustain lasing, the measured Q values were still less than 1000. In particular, the radiation losses were predominantly out of plane, while the in-plane losses were in comparison small [7]. Although refinements in design [11] and fabrication [12] had since increased the total measured Q to as high as 2,800, applications in cavity QED require Q values on the order of 10^4 to

achieve strong coupling (assuming $V_{\text{eff}} \sim (\lambda/n)^3$).

The limitations on Q stem from a number of possible factors, including intrinsic material absorption, etch-induced surface roughness and surface-state absorption, and other fabrication irregularities that prevent ideal replication of a given design. These issues aside, the fundamental design of these cavities had left room for improvement, and as such, the focus of this chapter primarily lies here. Our main objective is to consider simple design rules that can be used to significantly reduce the vertical losses from these structures, while maintaining or even improving upon the in-plane losses. In section 2.2, we describe a simple picture which illustrates that the vertical radiation loss of a mode is characterized by the presence of momentum components within the light cone of the cladding of the host slab waveguide (WG). We then consider (section 2.3) the use of symmetry to eliminate in-plane momentum components (\mathbf{k}_{\perp}) at $\mathbf{k}_{\perp} = 0$ (DC), thereby reducing the vertical loss in the structure. Drawing heavily from chapter 1, we summarize the different defect modes available in hexagonal and square lattice PCs, and proceed to choose target symmetries for modes in these lattices based upon the constraints they impose on the dominant field components of the modes. In section 2.4, we propose simple defect geometries that support such modes and present the results of three-dimensional (3D) finite-difference time-domain (FDTD) calculations of their relevant properties. In section 2.5, we consider further improvements in the designs based on a Fourier space tailoring of the defect geometries that reduces coupling of the mode's dominant Fourier components to components that radiate. The results of FDTD simulations of these improved designs in a square lattice are presented, and show that a modal Q -factor approaching 10^5 can be achieved by a careful consideration of the mode and defect geometry in Fourier space. Similar considerations are given in sections 2.6 and 2.7, where we consider the design of high- Q defect modes within standard and compressed hexagonal lattice photonic crystals. Comparable results in terms of Q ($\sim 10^5$) and V_{eff} ($\sim (\lambda/n)^3$) are achieved in these lattices.

2.2 Momentum space consideration of vertical radiation loss

The optical cavities studied here are comprised of defects situated in 2D PC slab WGs (fig. 2.1). As a result, the in-plane confinement of the cavity modes is governed by the distributed Bragg reflection (DBR) of the surrounding photonic lattice. Leakage of light in the plane of the PC slab WG from the cavity is thus determined by the number of periods of the host lattice surrounding the defect and the width and angular extent of the in-plane guided mode bandgap. Vertical confinement, on the

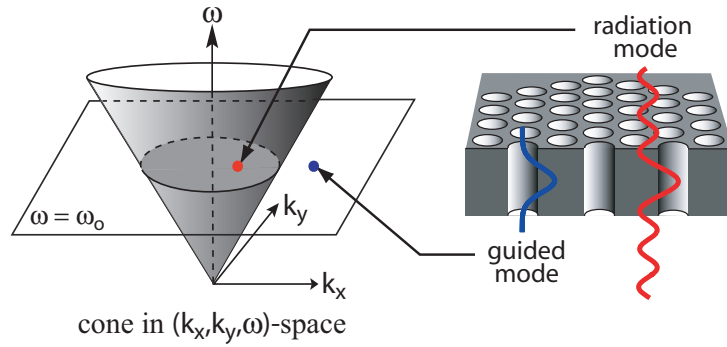


Figure 2.1: 2D hexagonal PC slab waveguide structure and cladding light cone.

other hand, is due to standard waveguiding by total internal reflection. Vertical radiation loss occurs when the magnitude of the in-plane momentum component, k_{\perp} , is inappropriate to support guiding. More concretely, we note that the energy-momentum dispersion relationship for a homogenous dielectric cladding (refractive index n) of the PC slab WG is $(n\omega/c)^2 = k_{\perp}^2 + k_z^2$, where ω is the angular frequency, k_z is the momentum normal to the slab, and c is the speed of light. For an air clad PC WG as studied here, $k_{\perp}^2 = (\omega/c)^2$ defines a cone in (k_x, k_y, ω) space, commonly referred to as the “light cone” (fig. 2.1). Modes that radiate vertically will have small in-plane momentum components that lie within the light cone of the cladding, thereby creating an oscillatory (radiating) field in the air instead of an evanescently decaying field. Equivalently, from a ray optics perspective, modes with in-plane momenta lying within the cladding light cone do not meet the total internal reflection condition at the semiconductor-air interface. This simple rule serves as our fundamental guideline in designing cavities that limit vertical radiation loss. In particular, we seek out structures that support resonant modes whose in-plane momentum components are primarily situated outside of the cladding light cone.

Before discussing methods to improve the vertical loss properties of PC defect cavities, it is instructive to consider the characteristics of the previously studied [7] dipole-like defect modes in a hexagonal lattice PC. Consider the x -dipole donor mode produced by a symmetric defect consisting of the removal of a single air hole from a hexagonal lattice of air holes in a 2D slab WG, as discussed in the previous chapter. Following the symmetry analysis presented in chapter 1, we see that this mode is composed of dominant Fourier components directed along $\pm\{\mathbf{k}_{X_1}, \mathbf{k}_{X_2}, \mathbf{k}_{X_3}\}$, where the \mathbf{k}_X directions are shown in the hexagonal PC reciprocal space lattice of fig. 2.2(a). The 2D spatial Fourier Transform (FT) of the x -dipole field component \mathbf{E}_x at the middle of the PC slab WG is given

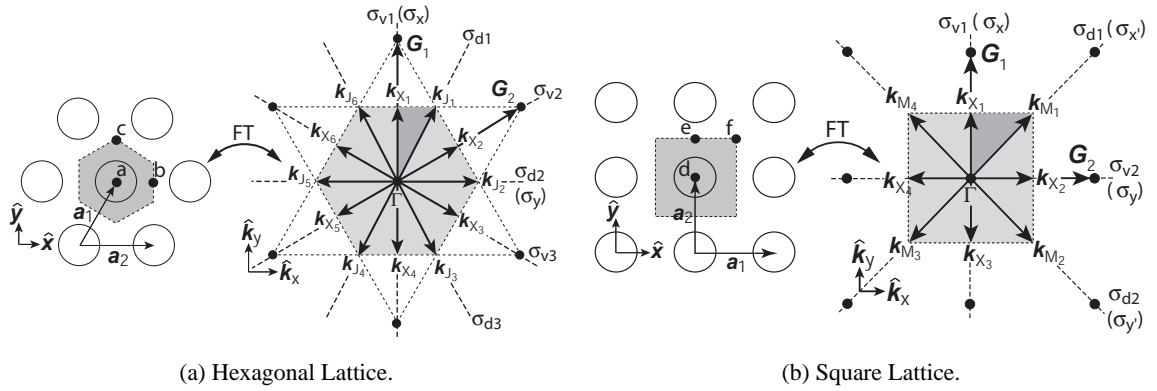


Figure 2.2: Real and reciprocal space lattices of (a) a 2D hexagonal lattice, and (b) a 2D square lattice. For the hexagonal lattice: $|\mathbf{a}_1| = |\mathbf{a}_2| = a$, $|\mathbf{G}_1| = |\mathbf{G}_2| = 4\pi/\sqrt{3}a$, $|\mathbf{k}_X| = 2\pi/\sqrt{3}a$, $|\mathbf{k}_J| = 4\pi/3a$. For the square lattice: $|\mathbf{a}_1| = |\mathbf{a}_2| = a$, $|\mathbf{G}_1| = |\mathbf{G}_2| = 2\pi/a$, $|\mathbf{k}_X| = \pi/a$, $|\mathbf{k}_M| = \sqrt{2}\pi/a$.

in fig. 2.3(a). It shows the E -field to be primarily composed of momentum components located about the X points, with $\pm\mathbf{k}_{X_1}$ as the strongest components. Note that the field has a significant amplitude for momentum components lying within the light cone, the boundary of which is shown in fig. 2.3(a) as a dashed white circle. These low momentum components radiate and are the cause of the mode's relatively low effective vertical Q -factor ($Q_{\perp} \approx 1000$).

2.3 Summary of the symmetry analysis of defect modes in hexagonal and square lattices

There are a number of ways to limit the presence of small in-plane momentum components in the localized resonant modes of PC slab WG defect cavities. For example, the geometry of the defect and the surrounding holes can be tailored to reduce the magnitude of these components, as was done in ref. [11], where the authors report a predicted Q of 30,000. One particularly appealing way to limit the presence of small in-plane momentum components is to use symmetry to enforce specific boundary conditions on the Fourier space representation of the mode. A defect will support one or more resonant modes with symmetries that are compatible with the nature of the defect and the surrounding PC. Of particular interest are modes whose symmetry is odd about mirror planes normal to the dominant Fourier components of the mode. In the context of our symmetry analysis, the fields of the approximate TE-like modes have in-plane electric field polarization normal

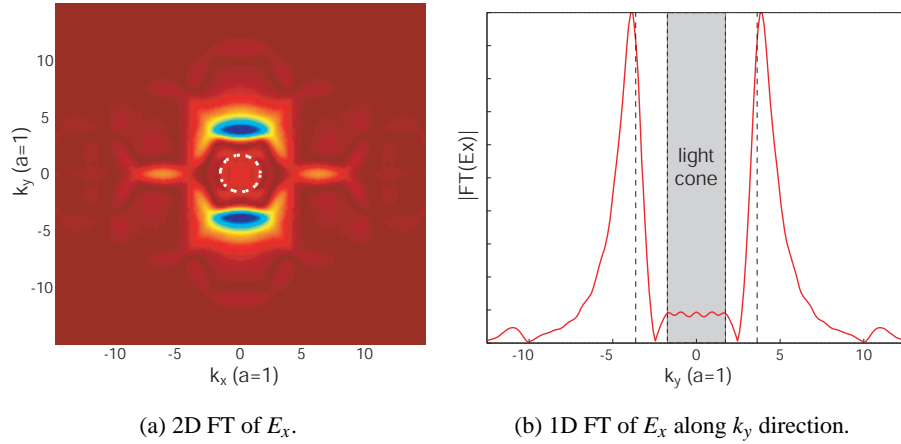


Figure 2.3: Spatial FT of x -dipole donor mode in a hexagonal lattice ($r/a = 0.30$) with a central missing air hole. (a) in 2D, (b) along the k_y direction with $k_x = 0$.

to the direction of their dominant Fourier components. In Fourier space, our choice of symmetry is equivalent to eliminating these in-plane electric field polarizations at $\mathbf{k}_\perp = 0$ (DC). This elimination of DC momentum components is the first step in reducing vertical radiation loss, and serves as our fundamental criterion for choosing the desired symmetry for our defect modes.¹ In addition, as we shall discuss later within this thesis (chapter 4), this use of a symmetry as a primary mechanism for reducing vertical radiation loss is also important from the standpoint of making cavities whose Q s are relatively robust to perturbations in their geometries.

The defect modes of a PC cavity are generally classified into donor- and acceptor-type modes [94], based upon whether the defect creates modes from the conduction band edge (donor modes) or valence band edge (acceptor modes). For the hexagonal lattice, whose real and reciprocal space depictions are given in fig. 2.2(a), the valence band edge is at the J -point and the conduction band edge is at the X -point (fig. 2.4(a)), while the square lattice of fig. 2.2(b) has its valence band edge at the M -point and conduction band edge at the X -point (fig. 2.4(b)). The dominant Fourier components and symmetry of a defect mode are determined by the type of mode (donor or acceptor) under consideration, the symmetry of the surrounding PC lattice, and the point group symmetry of the defect. The use of such an analysis to produce approximate forms for the modes in hexagonal and square lattice PC defect cavities was the focus of section 1.1, and as a result, here, we primarily incorporate the results of that chapter and describe their implications towards the

¹This can be viewed in the far-field as elimination of lower-order multi-pole radiation components, as has been considered by Johnson and co-workers [108]

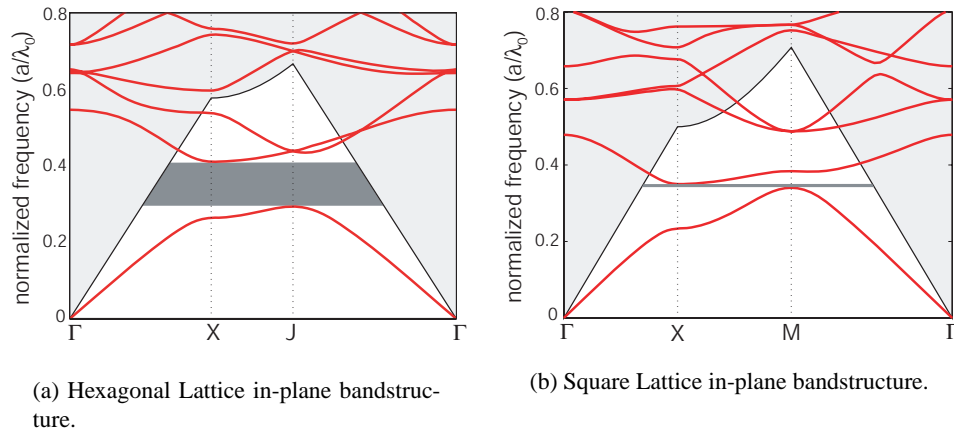


Figure 2.4: Fundamental TE-like (even) guided mode bandstructure for hexagonal and square lattices, calculated using a 2D plane-wave expansion method with an effective index for the vertical guiding: (a) hexagonal lattice with $r/a = 0.36$, $n_{\text{slab}} = n_{\text{eff}} = 2.65$, (b) square lattice with $r/a = 0.40$, $n_{\text{slab}} = n_{\text{eff}} = 2.65$.

design of high- Q defect resonators. The course of study is the following: we use the results of this group-theory-based analysis to determine the symmetry and dominant Fourier components for the available donor and acceptor type modes formed at different high symmetry points within hexagonal and square lattice PCs. Candidate modes for high- Q resonators are then chosen from these sets of available modes based upon the criteria placed on the mode's momentum components as described above. Within the mirror plane of the slab WG (coordinates \mathbf{r}_{\perp}) the TE modes are described by the field components \mathbf{E}_x , \mathbf{E}_y , and \mathbf{H}_z . Since the magnetic field is exactly scalar within this mirror plane, the criterion reduces to looking for modes in which the magnetic field pattern is spatially even in the directions of its dominant Fourier components. This is equivalent to having the in-plane electric field components spatially odd in these directions.

2.3.1 Hexagonal lattice

For a hexagonal lattice, the high symmetry points about which a defect may be formed are points a (C_{6v} symmetry), b (C_{2v} symmetry), and c (C_{3v,σ_v} symmetry) shown in fig. 2.2(a). Here, we consider donor and acceptor modes formed only at points a and b , as from the analysis presented in the previous chapter, those centered at point c do not contribute modes with the requisite symmetry and dominant Fourier components. We also examine reduced symmetry modes formed at point a , where the reduction of symmetry from C_{6v} to C_{2v} is accomplished by choosing a defect that

Table 2.1: Symmetry classification and dominant Fourier components for the \mathbf{H} -field of conduction band donor modes in a hexagonal lattice.

Defect Center	C_{6v} Modes	Fourier Comp.	$(\sigma_d, \sigma_v)^a$	C_{2v} Modes	$(\sigma_x, \sigma_y)^a$
(0,0)	$\mathbf{H}_{B_1}^{a,d1}$	$\pm\{\mathbf{k}_{X_1}, \mathbf{k}_{X_2}, \mathbf{k}_{X_3}\}$	(+, -)	$\mathbf{H}_{B_1}^{a,d1,1}$	(-, +)
(0,0)	$\mathbf{H}_{E_1,1}^{a,d1}$	$\pm\{\mathbf{k}_{X_1}, \mathbf{k}_{X_2}, \mathbf{k}_{X_3}\}$	(0,0)	$\mathbf{H}_{B_1}^{a,d1,2}$	(-, +)
(0,0)	$\mathbf{H}_{E_1,2}^{a,d1}$	$\pm\{\mathbf{k}_{X_2}, \mathbf{k}_{X_3}\}$	(0,0)	$\mathbf{H}_{B_2}^{a,d1}$	(+, -)
($a/2,0$)	N/A ^b	$\pm\{\mathbf{k}_{X_2}, \mathbf{k}_{X_3}\}$	N/A	$\mathbf{H}_{A_1}^{b,d1}$	(+, +)
($a/2,0$)	N/A	$\pm\{\mathbf{k}_{X_2}, \mathbf{k}_{X_3}\}$	N/A	$\mathbf{H}_{A_2}^{b,d1}$	(-, -)
($a/2,0$)	N/A	$\pm\{\mathbf{k}_{X_1}\}$	N/A	$\mathbf{H}_{B_1}^{b,d1}$	(-, +)

^a Character values.

^b Not applicable. Modes centered at point b are of C_{2v} symmetry.

breaks the symmetry of the lattice and is compatible with C_{2v} . Based upon the analysis of chapter 1, we create table 2.1 for donor modes and table 2.2 for acceptor modes. These tables provide the labeling scheme for the C_{6v} and C_{2v} modes, the dominant Fourier components of the modes, and their transformation properties about the available mirror planes (the mirror plane properties are represented by their character values [92]).

Donor modes of C_{6v} symmetry, formed at point a in the lattice, have their dominant Fourier components in the $\pm\{\mathbf{k}_{X_1}, \mathbf{k}_{X_2}, \mathbf{k}_{X_3}\}$ directions, and we thus require that $\sigma_d = -1$, where the σ_{d_i} are the mirror planes labeled in fig. 2.2(a). However, $\sigma_d \neq -1$ for the modes listed in table 2.1. Reducing the symmetry of the mode to C_{2v} (through a modified defect at point a or re-centering to point b) results in modes with dominant Fourier components that are not orthogonal to the available mirror planes, or as in the case of the $\mathbf{H}_{B_1}^{b,d1}$ mode, have incorrect spatial symmetry.

Out of the C_{6v} acceptor modes in table 2.2, the $\mathbf{H}_{A_2}^{a,a1}$ mode satisfies the symmetry criteria. The $\mathbf{H}_{A_2}^{b,a1}$ mode produced at position b does not quite satisfy our criteria, as two of the three pairs of dominant Fourier components ($\pm\{\mathbf{k}_{J_1}, \mathbf{k}_{J_3}\}$) are not orthogonal to the mirror planes; however, distortions of the lattice that preferentially select for the $\pm\mathbf{k}_{J_5}$ Fourier components over $\pm\mathbf{k}_{J_1}$ and $\pm\mathbf{k}_{J_3}$ can be made so that the symmetry condition is satisfied. Such lattice distortions are addressed in section 2.7. As a reference, the approximate form for the $\mathbf{H}_{A_2}^{a,a1}$ mode, given previously in equation (1.20), is listed below:

Table 2.2: Symmetry classification and dominant Fourier components for the \mathbf{H} -field of valence band acceptor modes in a hexagonal lattice.

Defect Center	C_{6v} Modes	Fourier Comp.	(σ_d, σ_v)	C_{2v} Modes	(σ_x, σ_y)
(0,0)	$\mathbf{H}_{A_2''}^{a,a1}$	$\pm\{\mathbf{k}_{J_1}, \mathbf{k}_{J_3}, \mathbf{k}_{J_5}\}$	(-, -)	$\mathbf{H}_{A_2}^{a,a1}$	(-, -)
(0,0)	$\mathbf{H}_{B_2''}^{a,a1}$	$\pm\{\mathbf{k}_{J_1}, \mathbf{k}_{J_3}, \mathbf{k}_{J_5}\}$	(-, +)	$\mathbf{H}_{B_2}^{a,a1}$	(+, -)
($a/2, 0$)	N/A	$\pm\{\mathbf{k}_{J_1}, \mathbf{k}_{J_3}, \mathbf{k}_{J_5}\}$	N/A	$\mathbf{H}_{A_2}^{b,a1}$	(-, -)
($a/2, 0$)	N/A	$\pm\{\mathbf{k}_{J_1}, \mathbf{k}_{J_3}, \mathbf{k}_{J_5}\}$	N/A	$\mathbf{H}_{B_2}^{b,a1}$	(+, -)

$$\mathbf{H}_{A_2''}^{a,a1} = \hat{z} \left(\cos(\mathbf{k}_{J_1} \cdot \mathbf{r}_\perp^a) + \cos(\mathbf{k}_{J_3} \cdot \mathbf{r}_\perp^a) + \cos(\mathbf{k}_{J_5} \cdot \mathbf{r}_\perp^a) \right), \quad (2.1)$$

where \mathbf{r}_\perp^a denotes in-plane coordinates referenced to point a .

2.3.2 Square lattice

The square lattice of air holes in a dielectric slab, whose real and reciprocal space representations are shown in fig. 2.2(b), and whose TE-mode bandstructure is depicted in fig. 2.4(b), also provides a photonic lattice from which low-loss defect modes can be formed. Defects in a square lattice may be centered at the C_{4v} symmetry points d and f , or the C_{2v} symmetry point e . Again, following the analysis of chapter 1, we produce tables 2.3 and 2.4 for the square lattice defect modes.

Based on their properties under mirror reflection, the $\mathbf{H}_{A_2''}^{f,d1}$, $\mathbf{H}_{B_2''}^{f,d1}$, and $\mathbf{H}_{A_2}^{e,d1}$ donor modes all meet the symmetry condition we have placed on the modes. By suitable modification of the defect geometry, the symmetry of modes formed at points d and f can be reduced to C_{2v,σ_v} or C_{2v,σ_d} , where the subscript σ_v denotes symmetry with respect to the (σ_x, σ_y) mirror planes and the subscript σ_d refers to the $(\sigma_{x'}, \sigma_{y'})$ mirror planes (fig. 2.2(b)). The modes at f continue to satisfy the symmetry criteria under C_{2v,σ_v} , but no longer do so under C_{2v,σ_d} , as the σ_d mirror planes are not orthogonal to the modes' dominant Fourier components.

The acceptor states formed from the valence band edge at the M -point are analyzed in a similar fashion, and in this case, the modes at points d and f are candidates. The reduced symmetry C_{2v,σ_v} modes at points d and f are ruled out, while the C_{2v,σ_d} modes at these two high symmetry points

Table 2.3: Symmetry classification and dominant Fourier components for the \mathbf{H} -field of conduction band donor modes in a square lattice.

Defect center	C_{4v}	Fourier Comp.	(σ_d, σ_v)	C_{2v, σ_v}	(σ_x, σ_y)	C_{2v, σ_d}	$(\sigma_{x'}, \sigma_{y'})$
(0,0)	$\mathbf{H}_{E,1}^{d,d1}$	$\pm\{\mathbf{k}_{X_1}\}$	(0,0)	$\mathbf{H}_{B_1}^{d,d1}$	(-,+)	$\mathbf{H}_{B'_1}^{d,d1}$	(-, -)
(0,0)	$\mathbf{H}_{E,2}^{d,d1}$	$\pm\{\mathbf{k}_{X_2}\}$	(0,0)	$\mathbf{H}_{B_2}^{d,d1}$	(+,-)	$\mathbf{H}_{B'_2}^{d,d1}$	(+, -)
($a/2, a/2$)	$\mathbf{H}_{A_2''}^{f,d1}$	$\pm\{\mathbf{k}_{X_1}, \mathbf{k}_{X_2}\}$	(-, -)	$\mathbf{H}_{A_2}^{f,d1,1}$	(-, -)	$\mathbf{H}_{A_2'}^{f,d1}$	(-, -)
($a/2, a/2$)	$\mathbf{H}_{B_2''}^{f,d1}$	$\pm\{\mathbf{k}_{X_1}, \mathbf{k}_{X_2}\}$	(-, +)	$\mathbf{H}_{A_2}^{f,d1,2}$	(-, -)	$\mathbf{H}_{A_1'}^{f,d1}$	(-, -)
(0, $a/2$)	N/A ^a	$\pm\{\mathbf{k}_{X_1}\}$	N/A	$\mathbf{H}_{A_2}^{e,d1}$	(-, -)	N/A	N/A
(0, $a/2$)	N/A	$\pm\{\mathbf{k}_{X_2}\}$	N/A	$\mathbf{H}_{B_2}^{e,d1}$	(+, -)	N/A	N/A

^a Not applicable. Modes centered at point e are of C_{2v} symmetry.

Table 2.4: Symmetry classification and dominant Fourier components for the \mathbf{H} -field of valence band acceptor modes in a square lattice.

Defect Center	C_{4v}	Fourier Comp.	(σ_d, σ_v)	C_{2v, σ_v}	(σ_x, σ_y)	C_{2v, σ_d}	$(\sigma_{x'}, \sigma_{y'})$
(0,0)	$\mathbf{H}_{A_2''}^{d,a1}$	$\pm\{\mathbf{k}_{M_1}, \mathbf{k}_{M_2}\}$	(-, -)	$\mathbf{H}_{A_2}^{d,a1}$	(-, -)	$\mathbf{H}_{A_2'}^{d,a1}$	(-, -)
($a/2, a/2$)	$\mathbf{H}_{B_1''}^{f,a1}$	$\pm\{\mathbf{k}_{M_1}, \mathbf{k}_{M_2}\}$	(+, -)	$\mathbf{H}_{A_1}^{f,a1}$	(+, +)	$\mathbf{H}_{A_2'}^{f,a1}$	(-, -)
(0, $a/2$)	N/A	$\pm\{\mathbf{k}_{M_1}, \mathbf{k}_{M_2}\}$	N/A	$\mathbf{H}_{B_1}^{e,a1}$	(-, +)	N/A	N/A

remain on the list. As a reference, the approximate forms for the candidate donor and acceptor modes are given in table 2.5 below.

Table 2.5: Candidate donor and acceptor modes in a square lattice.

Donor Modes	Acceptor Modes
$\mathbf{H}_{A_2''}^{f,d1} = \hat{z}(\cos(\mathbf{k}_{X_1} \cdot \mathbf{r}_{\perp}^f) + \cos(\mathbf{k}_{X_2} \cdot \mathbf{r}_{\perp}^f))$	$\mathbf{H}_{A_2''}^{d,a1} = \hat{z}(\cos(\mathbf{k}_{M_1} \cdot \mathbf{r}_{\perp}^d) + \cos(\mathbf{k}_{M_2} \cdot \mathbf{r}_{\perp}^d))$
$\mathbf{H}_{B_2''}^{f,d1} = \hat{z}(\cos(\mathbf{k}_{X_1} \cdot \mathbf{r}_{\perp}^f) - \cos(\mathbf{k}_{X_2} \cdot \mathbf{r}_{\perp}^f))$	$\mathbf{H}_{B_1''}^{f,a1} = \hat{z}(\cos(\mathbf{k}_{M_1} \cdot \mathbf{r}_{\perp}^f) - \cos(\mathbf{k}_{M_2} \cdot \mathbf{r}_{\perp}^f))$
$\mathbf{H}_{A_2}^{e,d1} = \hat{z}(\cos(\mathbf{k}_{X_1} \cdot \mathbf{r}_{\perp}^e))$	

2.4 Initial FDTD simulation results

The symmetry analysis presented in the previous section determined the modes satisfying our symmetry criteria, chosen to reduce vertical radiation losses from the PC slab WG. For a hexagonal lattice, we singled out the acceptor mode of equation (2.1), while for the square lattice, a number of options were available, as summarized in table 2.5. We begin the 3D FDTD analysis of high- Q PC resonant cavities by choosing particular defects in the hexagonal and square lattices that will support one of these modes. Results from the FDTD analysis will provide a measure of the benefits obtained in using modes of such symmetries, and will also give an indication of what further improvements are needed. This will lead naturally to the Fourier space tailoring of the lattice discussed in sections 2.5 and 2.6.

The FDTD calculations presented in this section (see appendix B for more details) were performed on a mesh with 20 points per lattice spacing (greater than 70 points per free space wavelength or 20 points per wavelength in the dielectric). Cavity modes were excited by an initial field (H_z) with a localized Gaussian profile, and even modes of the slab WG were preferentially selected by using an even mirror symmetry condition ($\sigma_h = 1$) in the middle of the slab. In order to maintain a single vertical mode of the PC slab waveguide (within the frequency band of interest), we choose a normalized slab thickness $d/a = 0.75$ in this section. Where appropriate, the mirror planes (σ_x, σ_y) were used to filter out cavity modes according to their projection onto the irreducible representations (IRREPs) of C_{2v, σ_v} . Mur's absorbing boundary conditions were used to terminate the FDTD simulation domain in all other directions. Q values are calculated by determining the power absorbed in the boundaries (P_{abs}) and the stored energy in the mode (U), and taking $Q = \omega_0 U / P_{abs}$, where ω_0 is the angular frequency of the mode. By distinguishing between power flow to vertical

and in-plane boundaries, effective Q values Q_{\perp} and Q_{\parallel} are calculated, with the total quality factor being determined by $1/Q = 1/Q_{\parallel} + 1/Q_{\perp}$ [7]. It should be noted that a number of other methods were also used to estimate the Q values, including the modal energy decay rate and the radiated power calculated from the near field momentum components lying within the cladding light cone, all resulting in consistent values. The effective volume [109, 110] of the cavity modes, V_{eff} in the tables below, is calculated using the peak in the electric field energy density and is given in units of cubic wavelengths in the material.² The explicit form of V_{eff} is:

$$V_{\text{eff}} = \frac{\int_V \epsilon(\mathbf{r}) |\mathbf{E}(\mathbf{r})|^2 d^3\mathbf{r}}{\max[\epsilon(\mathbf{r}) |\mathbf{E}(\mathbf{r})|^2]} \quad (2.2)$$

2.4.1 Hexagonal lattice

The $\mathbf{H}_{A_2''}^{a,a1}$ mode, our candidate mode for study, is formed by enlarging holes in a manner consistent with the C_{6v} symmetry of the lattice, so that an acceptor mode is formed. We choose the defect geometry shown in table 2.6, where the central hole (about point a) is enlarged from radius r to r' . The defect is surrounded by a total of 8 periods of the hexagonal lattice in the \hat{x} -direction and 12 periods in the \hat{y} -direction. The magnetic field amplitude and Fourier-transformed momentum space electric field components $\tilde{\mathbf{E}}_x$ and $\tilde{\mathbf{E}}_y$ of mode $\mathbf{H}_{A_2''}^{a,a1}$ are given in table 2.6 for two different pairs of values (r, r') . The dominant Fourier components are seen to be $\pm\{\mathbf{k}_{J_1}, \mathbf{k}_{J_3}, \mathbf{k}_{J_5}\}$, as predicted by the symmetry analysis. Examining $\tilde{\mathbf{E}}_x$ and $\tilde{\mathbf{E}}_y$, it is also clear that, although the power within the light cone has been reduced in comparison to the x -dipole donor mode, it is still significant. This fact is evidenced in Q_{\perp} which, at 4,900 for $r/a = 0.35$ and $r'/a = 0.45$, is larger than that obtained for the x -dipole mode. By reducing the frequency, and consequently the radius of the light cone, the PC cavity with $r/a = 0.30$ and $r'/a = 0.45$ has an improved vertical Q of 8,800 (although its in-plane Q has degraded due to a reduction in the in-plane bandgap for smaller lattice hole radii).

²In our original papers [21, 23], we quoted modal volumes in terms of cubic wavelengths in air (λ^3); this unit has meaning in terms of describing the physical volume of the field. However, to compare differing cavity geometries across different material systems, the unit of cubic wavelengths in the material ($(\lambda/n)^3$) is more appropriate, and I have thus chosen this unit for all of the V_{eff} values quoted in this chapter and the rest of the thesis. In addition, certain phenomena, such as the enhanced radiative rate of an emitter within a cavity (the Purcell effect) are most straightforwardly calculated when the volume is quoted in units of $(\lambda/n)^3$. In other works within the field, mode volumes will sometimes be quoted in terms of cubic half-wavelength in the material ($(\lambda/2n)^3$), to provide a comparison against a theoretical cavity that can confine an optical mode to a half-wavelength in the material in all three dimensions (i.e., the optical analog of the particle in a 3D infinite square well from quantum mechanics).

Table 2.6: Characteristics of the $\mathbf{H}_{A_2'}^{a,a1}$ resonant mode in a hexagonal lattice (images are for a PC cavity with $r/a = 0.35$, $r'/a = 0.45$, $d/a = 0.75$, and $n_{\text{slab}} = 3.4$).

Geometry		$ \mathbf{H} $	$ \tilde{\mathbf{E}}_x $	$ \tilde{\mathbf{E}}_y $		
r/a	r'/a	$\omega_n = a/\lambda_o$	Q_{\parallel}	Q_{\perp}	Q_{tot}	$V_{\text{eff}}((\lambda/n)^3)$
0.35	0.45	0.265	34,100	4,900	4,300	0.54
0.30	0.45	0.248	5,300	8,800	3,300	0.84

2.4.2 Square lattice

We choose the $\mathbf{H}_{A_2}^{e,d1}$ mode as our candidate for study. This mode, centered in the dielectric at point e in the lattice, is appealing in that it has Fourier components primarily situated at $\pm\mathbf{k}_{X_1}$, while the other modes of correct symmetry have a larger number of Fourier components. This simplifies the design considerations of section 2.5. To create the mode, we consider the structure depicted in table 2.7. Defining point e as the origin, $(0,0)$, we see that the structure consists of a standard square lattice of air holes in which the two holes centered at $(0, \pm a/2)$ are decreased in size so as to create a donor mode of A_2 symmetry. In the FDTD simulations, the structure consists of 12 rows and 8 columns of air holes surrounding the defect holes.

Starting with $r/a = 0.30$, $r'/a = 0.28$, and $d/a = 0.75$, we produce a mode with normalized frequency $\omega_n = a/\lambda_o = 0.264$. The magnetic field amplitude and 2D spatial FTs ($\tilde{\mathbf{E}}_x$ and $\tilde{\mathbf{E}}_y$) of the mode are given in table 2.7. As the amplitude of $\tilde{\mathbf{E}}_y$ is small in comparison to that of $\tilde{\mathbf{E}}_x$, the mode is predominantly made up of components centered at $\pm\mathbf{k}_{X_1}$, as predicted. The effective vertical Q of this mode is approximately 54,000, easily exceeding the values obtained in ref. [8] for a mode of even symmetry. The small Q_{\parallel} (17,400) is a result of the weak defect perturbation and extended nature of the cavity mode ($V_{\text{eff}} = 2.11(\lambda/n)^3$). Improving the localization of the mode by lowering r'/a of the defect to 0.25 improves Q_{\parallel} to a value of 60,000 and lowers V_{eff} by a factor of almost two. Surprisingly, Q_{\perp} has also increased from 54,000 to 69,000 despite the stronger localization of the mode and its expected broadening in Fourier space. This rather counterintuitive result indicates

Table 2.7: Characteristics of the $\mathbf{H}_{A2}^{e,d1}$ resonant mode in a square lattice (images are for a PC cavity with $r/a = 0.30$, $r'/a = 0.28$, $d/a = 0.75$, and $n_{\text{slab}} = 3.4$).

Geometry		$ \mathbf{H} $	$ \tilde{\mathbf{E}}_x $	$ \tilde{\mathbf{E}}_y $		
\mathbf{r}/\mathbf{a}	\mathbf{r}'/\mathbf{a}	ω_n	Q_{\parallel}	Q_{\perp}	Q_{tot}	$\mathbf{V}_{\text{eff}}((\lambda/n)^3)$
0.30	0.28	0.265	17,400	54,000	13,000	2.11
0.30	0.25	0.262	60,100	69,200	32,000	1.08

that a more detailed study of the effects of the defect geometry on cavity loss is required. This is the focus of the following section.

2.5 Momentum space design of the defect geometry in a square lattice

The results for the simple square lattice cavities studied in the previous section are quite encouraging, and we will thus begin by examining cavity design within these square lattice structures before returning to the hexagonal lattice in a later section. The results given thus far indicate that improving the loss properties of the defect mode resonators requires isolation of the mode's momentum components to regions outside the light cone to maintain a high Q_{\perp} , and to those regions for which the in-plane bandgap is substantial for a high Q_{\parallel} . To determine how to tailor the defect geometries to accomplish these goals, we consider a simple model to illustrate the couplings induced in Fourier space between the dominant momentum components of a given defect mode and those modes which radiate. We employ a two-step process where in the first step, the approximate form of the defect mode is taken based on symmetry arguments, as outlined in section 2.3, with the allowance for finite \mathbf{k} -space bandwidths in the dominant Fourier components due to the localization of the defect mode. We then consider couplings of this approximate symmetry mode to other modes of the PC slab WG through the dielectric perturbation $\Delta\eta(\mathbf{r})$, where $\eta = 1/\epsilon$ is the inverse of the dielectric profile of the lattice. The most important mode couplings from the perspective of increasing the Q are those

between the dominant Fourier components and “leaky cavity modes.” The leaky cavity modes consist of vertical radiation modes and guided modes of the PC slab WG which are not reflected by the PC and thus leak in-plane. $\Delta\eta$ induces the change $\delta\mathbf{H}^d(\mathbf{r})$ in the defect mode, and this change is written as a superposition over the set of nearly (frequency) degenerate guided and radiation modes of the PC slab WG. The coupling amplitude between the symmetry mode composed of the dominant Fourier components, $\mathbf{H}_o^d(\mathbf{r})$, and a leaky cavity mode, $\mathbf{H}_o^{lcm}(\mathbf{r})$, of the unperturbed PC slab is given by the following matrix element:

$$\int d^3r \left(\mathbf{H}_o^{lcm}(\mathbf{r}) \right)^* \left(\nabla \times \left(\Delta\eta(\mathbf{r}) \nabla \times \mathbf{H}_o^d(\mathbf{r}) \right) \right) \sim \int \frac{d^2k_\perp}{(2\pi)^4} \left(\tilde{H}_{z,o}^{lcm} \right)^* \left(\left[\tilde{\Delta\eta} * (|\mathbf{k}_\perp|^2 \tilde{H}_{z,o}^d) \right] + \left[(k_x \tilde{\Delta\eta}) * (k_x \tilde{H}_{z,o}^d) \right] + \left[(k_y \tilde{\Delta\eta}) * (k_y \tilde{H}_{z,o}^d) \right] \right) \quad (2.3)$$

where $*$ denotes convolution. In converting from the real space integral to momentum space, we have neglected the variation of $\eta(\mathbf{r})$ and $\Delta\eta(\mathbf{r})$ in the \hat{z} -direction, so that $\mathbf{H}_o^d(\mathbf{r}) \approx H_{z,o}^d(\mathbf{r}_\perp)$ (TE-like mode). From this equation, it is clear that the Fourier Transform of the dielectric perturbation, $\tilde{\Delta\eta}(\mathbf{k}_\perp)$, is the key quantity that couples Fourier components between the basis modes of the system. By tailoring this quantity appropriately, we can thus limit couplings that lead to in-plane and vertical leakage.

The formula given above is meant to be a qualitative guide to help build physical intuition; it is not a rigorous formula that can be expected to be quantitatively accurate. Such a formula can be conceived, however, by considering the Wannier analysis provided in the previous chapter. In particular, in equation (1.58), we showed that the mixing of the Bloch modes of the PC due to the presence of the defect perturbation, $\hat{L}'_H = -\nabla(\Delta\eta) \cdot \nabla - (\Delta\eta)\nabla^2$, is given by:

$$\langle H_{l',\mathbf{k}'} | \hat{L}'_H H_{l,\mathbf{k}} \rangle = \sum_{\mathbf{G}} \sum_{\mathbf{k}''} \left(\tilde{\Delta\eta}_{\mathbf{k}''} K_{l',l}(\mathbf{k}', \mathbf{k}, \mathbf{G}) + \tilde{\Delta\eta}_{\mathbf{k}''}(i\mathbf{k}'') \cdot \mathbf{L}_{l',l}(\mathbf{k}', \mathbf{k}, \mathbf{G}) \right) \delta_{\mathbf{k}' - \mathbf{k}'' + \mathbf{G}, \mathbf{k}}, \quad (2.4)$$

where $\tilde{\Delta\eta}_{\mathbf{k}''}$ is the \mathbf{k}'' th Fourier coefficient of $\Delta\eta(\mathbf{r})$, l and \mathbf{k} label the band index and crystal momentum of the $H_{l,\mathbf{k}}$ Bloch wave, the \mathbf{G} are reciprocal lattice vectors, and $K_{l',l}(\mathbf{k}', \mathbf{k}, \mathbf{G})$ and $\mathbf{L}_{l',l}(\mathbf{k}', \mathbf{k}, \mathbf{G})$ are scalar and vector coupling matrix elements, respectively, which depend upon the Bloch waves. As expected, this formula indicates the importance of the Fourier transform of the dielectric perturbation, $\tilde{\Delta\eta}(\mathbf{k}_\perp)$, in determining the coupling of different Bloch modes of the unperturbed crystal.

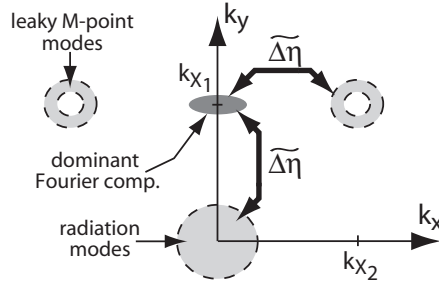


Figure 2.5: Illustration showing the mode coupling for the $\mathbf{H}_{A2}^{e,d1}$ mode in \mathbf{k} -space through the $\widetilde{\Delta\eta}$ perturbation.

Our candidate mode within the square lattice, $\mathbf{H}_{A2}^{e,d1}$, has dominant in-plane Fourier components at $\pm\mathbf{k}_{X1}$. We must therefore modify the defect so that $\widetilde{\Delta\eta}$ does not couple the $\pm\mathbf{k}_{X1}$ momentum components to those regions in \mathbf{k} -space which are “leaky.” In order to reduce radiation normal to the PC slab through coupling to the light cone, the amplitude of $\widetilde{\Delta\eta}$ in the neighborhood of $k_y = \pm\pi/a$ should be minimized. In addition, for the square lattice designs investigated here the bandgap between the conduction band edge at the X -point and the valence band edge at the M -point is at best very narrow, consequently, we look to reduce coupling between neighborhoods surrounding the X - and M -points. This implies that it will also be necessary to reduce the amplitude of $\widetilde{\Delta\eta}$ in the region about $k_x = \pm\pi/a$.

The crux of the argument described above is depicted in fig. 2.5, where lossy couplings are illustrated for the upper region of \mathbf{k} -space (the negative k_y region will behave identically in this case). Here we have assumed that the defect mode frequency lies below the conduction band edge at the X -point but slightly within the valence band near the M -point, resulting in an annular region of \mathbf{k} -space about the M -point which is strongly coupled to. With reference to this simple schematic, the Fourier components of $\widetilde{\Delta\eta}$ that lead to radiation losses from the defect cavity are approximately:

$$\begin{aligned} \widetilde{\Delta\eta} \left(|k_x| \lesssim (k_{lc} + \Delta_x), |k_y \pm |\mathbf{k}_{X1}|| \lesssim (k_{lc} + \Delta_y) \right) &\implies \text{coupling to light cone,} \\ \widetilde{\Delta\eta} \left(|k_x \pm |\mathbf{k}_{X2}|| \lesssim \Delta_x, |k_y| \lesssim \Delta_y \right) &\implies \text{coupling to leaky } M\text{-point.} \end{aligned} \quad (2.5)$$

where k_{lc} is the radius of the light cone, and Δ_x and Δ_y are the widths of the dominant Fourier peaks in the \hat{k}_x - and \hat{k}_y -directions, respectively.

Before attempting any design modifications, we first consider the simple defect geometry stud-

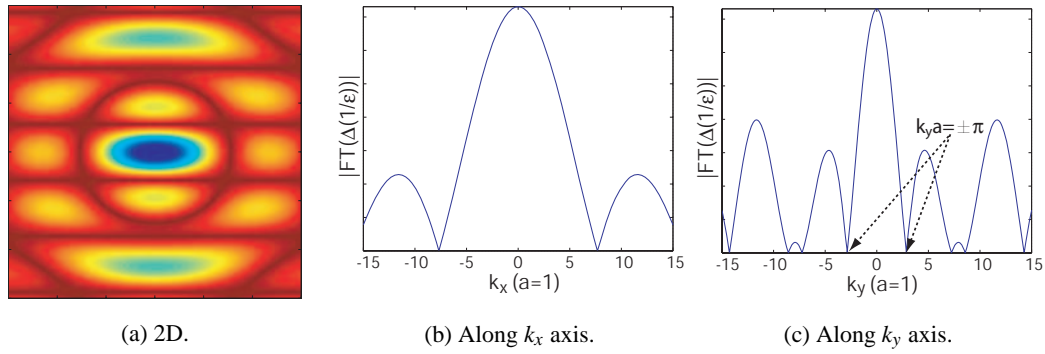


Figure 2.6: $\widetilde{\Delta\eta}(\mathbf{k}_\perp)$ for dielectric structure of table 2.7.

ied in section 2.4, where the holes located at $(0, \pm a/2)$ were reduced from the standard hole radius r to a radius r' . The perturbation $\Delta\eta$ is given by the difference in η with and without the defect holes, and thus simply consists of a pair of annuli, each of width $(r - r')$, centered at $(0, \pm a/2)$. The 2D spatial FT of this function can be obtained analytically [5], and is separable into the form

$$\widetilde{\Delta\eta}(\mathbf{k}_\perp) = F(k_\perp; r, r') \cos\left(\frac{k_y a}{2}\right), \quad (2.6)$$

where $F(k_\perp; r, r')$ is a function of the magnitude of the in-plane momentum, with r and r' as parameters. This function, along with one-dimensional (1D) slices along the k_x and k_y axes, is shown in fig. 2.6 (the figure shown is actually the direct FT of the structure used in FDTD calculations, to take into account any staircasing effects in the rendering of the holes; however, the difference between it and the analytic function are insignificant.). We notice, as is clear from examining equation (2.6), that $\widetilde{\Delta\eta} = 0$ at $k_y = \pm\pi/a$. Our choice of defect was thus a fortuitous one, as the zero amplitude of $\widetilde{\Delta\eta}$ at the X points eliminated coupling between the dominant Fourier components of the $\mathbf{H}_{A2}^{e,d1}$ mode and DC. Of course, a localized defect mode has a finite bandwidth in Fourier space about its dominant momentum components, and the light cone encompassing the radiation modes is of finite radius as well. As a result it is desirable to minimize the Fourier components of the dielectric perturbation over an extended region about $k_y = \pm\pi/a$. Note that $\widetilde{\Delta\eta}$ for the hexagonal lattice design of the previous section does not have zero amplitude at any of the \mathbf{k}_J , and thus the Q_\perp values are much smaller than those of the square lattice. To increase Q_\perp in the hexagonal lattice, future designs must therefore tailor the lattice in a way so that this amplitude is significantly reduced.

It is also necessary to modify the dielectric to improve Q_{\parallel} . The most straightforward way to immediately do so is to increase the r/a of the host PC, as that will provide a bandgap for an increased range of momentum values. This also tends to decrease Q_{\perp} , as the increased r/a will produce a mode of higher frequency, resulting in a cladding light cone of increased radius encompassing a larger range of momentum values. Fortunately, this does not necessarily have to hold for a general defect geometry. In particular, the hole radius can be kept relatively small in the region where the mode is primarily located, but can be graded outside this region to increase the in-plane reflectivity. The choice of grading can be determined by considering the need to limit the in-plane momentum components of the mode to regions in which the bandgap is substantial (note that for the simple two-hole design considered in section 2.4, $\widetilde{\Delta\eta}$ is quite large in this region of momentum space about $k_x = \pm\pi/a$). The benefit of this approach is that it does not necessarily result in increased vertical radiation loss, thus allowing for both a large Q_{\parallel} and Q_{\perp} .

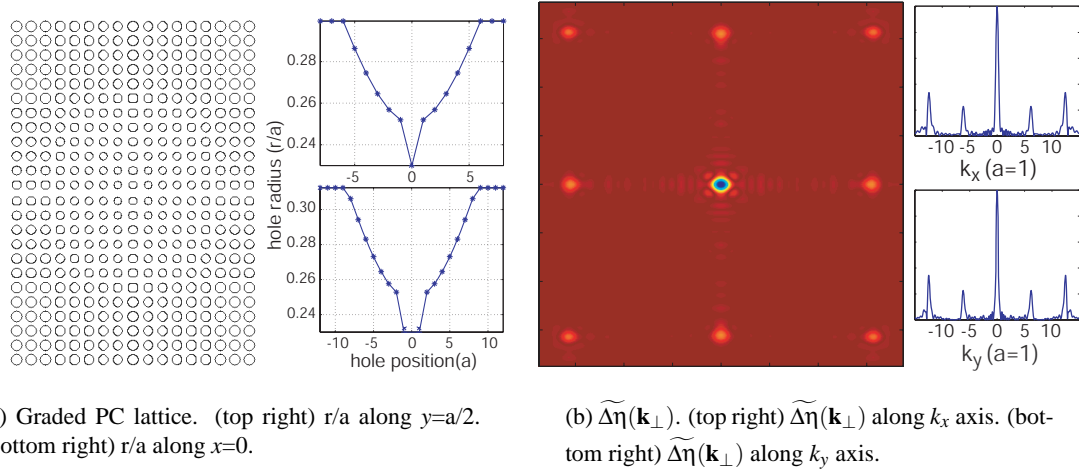
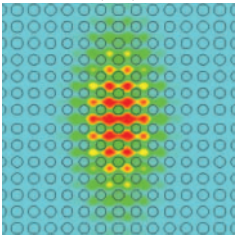
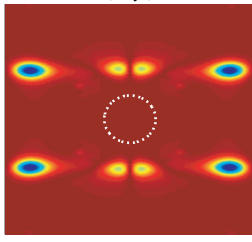
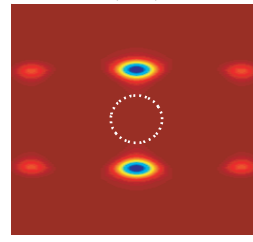
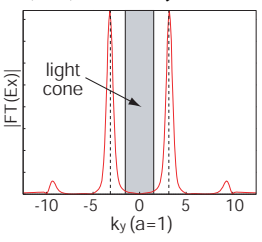


Figure 2.7: Properties of the graded square lattice.

Consider the graded lattice shown in fig. 2.7(a). The standard defect holes at $(0, \pm a/2)$ have $r/a = 0.23$, while their immediate neighbors have $r/a = 0.253$. The hole radii are then increased parabolically outwards for 5 periods in the \hat{x} -direction and 7 periods in the \hat{y} -direction, after which they are held constant. The nature of this grading is shown in fig. 2.7(a), where the r/a profiles are given for slices along $y = a/2$ and $x = 0$. Along these axes the maximum value r/a attains is 0.31, but along the diagonal directions r/a grows to be as large as 0.35. The dielectric perturbation, which now consists of a series of annuli of decreasing width from the center to the edges, has a FT

Table 2.8: Field characteristics of the graded square lattice shown in fig. 2.7(a).

$ \mathbf{H} $		$ \tilde{\mathbf{E}}_y $	$ \tilde{\mathbf{E}}_x $	$ \tilde{\mathbf{E}}_x $ along k_y axis	
					
\mathbf{d}/\mathbf{a}	ω_n	Q_{\parallel}	Q_{\perp}	Q_{tot}	$V_{\text{eff}}((\lambda/n)^3)$
0.75	0.245	470,000	110,000	89,000	1.23
0.85	0.239	422,000	128,000	98,000	1.28
0.95	0.235	296,000	139,000	95,000	1.33
1.05	0.231	280,000	145,000	96,000	1.38

given in fig. 2.7(b). Examining both the 2D image and the 1D line scans of the FT, we see that our grading has greatly diminished the amplitude of $\tilde{\Delta}\eta$ in the regions surrounding $k_y = \pm\pi/a$ and $k_x = \pm\pi/a$.

The FDTD simulations of the defect mode of this structure largely confirm the ideas described thus far. Q_{\perp} has increased to over 110,000, while Q_{\parallel} has improved even further to approximately 470,000, giving an overall $Q_{\text{tot}} \approx 89,000$. The predicted mode volume $V_{\text{eff}} \sim 1.2(\lambda/n)^3$, so that the combination of Q and V_{eff} achievable in this cavity is very promising from the standpoint of cavity QED experiments. This will be described in further detail in later chapters within this thesis.

The magnetic field amplitude and FT of the in-plane electric field components in table 2.8 provide further indication of the success of this design in suppressing radiation loss. In particular, consider the line scan of $\tilde{\mathbf{E}}_x$ along the k_y axis. It shows that the grading has met with success, as power has largely been eliminated within the light cone. This point is particularly striking when contrasted with the corresponding image shown in fig. 2.3(b) for the low Q x -dipole mode we took as our baseline. Note that $\tilde{\Delta}\eta(k_x = 0, k_y = \pm\pi/a)$ is identically zero regardless of the grade, due to the position of the defect holes with respect to the center of the defect, whereas $\tilde{\Delta}\eta(k_x = \pm\pi/a, k_y = 0)$ is not automatically zero. It may be advantageous to identically zero $\tilde{\Delta}\eta(k_x = \pm\pi/a, k_y = 0)$ as this will allow for the formation of a more localized mode that is still of high Q_{\parallel} . Such a mode would be centered at the f -point of the square lattice, and would either be the $\mathbf{H}_{A_2''}^{f,d1}$ or $\mathbf{H}_{B_2''}^{f,d1}$ mode.

Before concluding, there are a couple of points concerning the chosen lattice that are worth

mentioning. The first is that the initial jump in r/a between the defects at $(0, \pm a/2)$ and their neighbors is an important element of this design. Acting as a potential well, the jump helps confine the mode in real space, allowing r/a to increase quickly to a value for which the in-plane reflectivity is high without significantly increasing the modal frequency. The size of the jump is also important; if incorrectly sized the resulting dielectric perturbation contains larger Fourier amplitudes which couple the mode to the M -point for which the PC is no longer reflective and to the light cone in which light radiates vertically. An optimum defect design is found when a compromise is struck between the minimization of the Fourier components of $\widetilde{\Delta\eta}$ which couple the dominant momentum components of the defect mode to regions of \mathbf{k} -space which radiate, and the degree to which the dominant momentum components of the mode broaden due to in-plane confinement by the defect.

It should again be emphasized that the increased Q_{\perp} for these graded lattice designs is not solely the result of real-space delocalization of the mode, which has been an approach considered by other authors [108, 111]. It is instead largely due to the aforementioned reduction of amplitude for those Fourier components of the dielectric perturbation that couple the dominant momentum components of the defect mode to those which radiate. Of course, real-space localization plays a role in determining the spread in \mathbf{k} -space of the dominant Fourier components of the mode, and if this spread exceeds the size of the region about $\pm\mathbf{k}_{X_1}$ that $\widetilde{\Delta\eta}$ has been flattened, vertical radiation will result. An increase in the slab thickness also effects the performance of the structure. It causes a decrease in the frequency of the mode, thus increasing Q_{\perp} . It also slightly reduces the size of the in-plane bandgap, decreasing Q_{\parallel} . This is in fact seen in the results of FDTD simulations compiled in table 2.8.

Finally, we note that the criteria for choosing the geometries presented in this paper were entirely based on Q considerations, and optimization of the lattice grading to further increase Q can still be made. Changes may also be made to improve other aspects of the design. In particular, reducing the mode volume may be of importance to applications in quantum optics, while reducing the complexity of the design (in terms of the number and size of holes comprising the defect) may be of interest from a fabrication standpoint. Alternately, as we shall discuss in chapter 4, this graded lattice geometry is distinguished by supporting a mode whose Q is relatively insensitive to perturbations in the cavity geometry; one could envision making such robustness a prerequisite along with high- Q and small- V_{eff} in future designs of photonic crystal cavities. The approach to such designs can be aided through the Fourier space consideration of the dielectric perturbation as has been described in this section. Doing so will elucidate the potential lossy couplings that occur when the

defect mode is formed, and will help determine whether a given structure is able to sustain a high- Q mode.

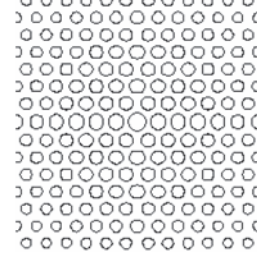
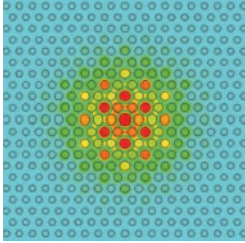
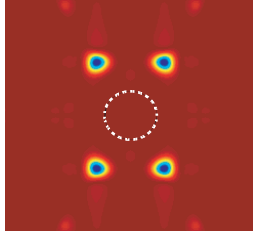
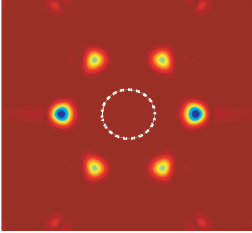
2.6 Tailoring of the defect geometry for the $\mathbf{H}_{A_2}^{a,a1}$ mode in the hexagonal lattice

When comparing defect modes of a square lattice with those of a hexagonal lattice in the context of forming high- Q microcavities, there are a number of salient points that merit consideration. The first is that the square lattice designs adopted above provided a natural “geometric” advantage in that $\widetilde{\Delta\eta}(\mathbf{k}_\perp)$ (even in the simplest case of two reduced size air holes) was automatically zero at the dominant Fourier components ($k_x = 0, k_y = \pm\pi/a$), thereby reducing coupling between those components and small momentum components that radiate. Furthermore, these dominant Fourier components were in directions orthogonal to the available mirror planes of the system, maximizing the symmetry-based reduction of small momentum components as discussed in section 2.2. In the hexagonal lattice, it is difficult to obtain a similar set of circumstances. The only mode consistent with the symmetry criteria is the $\mathbf{H}_{A_2}^{a,a1}$ mode, but defects that create such a mode have $\widetilde{\Delta\eta}(\mathbf{k}_\perp)$ that is non-zero at the mode’s dominant Fourier components ($\pm\{\mathbf{k}_{J_1}, \mathbf{k}_{J_3}, \mathbf{k}_{J_5}\}$). Conversely, a mode such as $\mathbf{H}_{A_2}^{b,d1}$, formed by a defect such as two reduced size holes at $(0, \pm a\sqrt{3}/2)$, could have $\widetilde{\Delta\eta}(\mathbf{k}_\perp) = 0$ at its dominant Fourier components ($\pm\{\mathbf{k}_{X_2}, \mathbf{k}_{X_3}\}$), but these Fourier components are oriented along directions that are not orthogonal to the available mirror planes of the system.

Despite these potential obstacles, it is certainly possible to design high- Q defect cavities in a hexagonal lattice. One advantage of the hexagonal lattice is that it exhibits a relatively large and complete in-plane bandgap for TE-like modes due to its nearly circular first Brillouin zone (IBZ) boundary. This essentially guarantees the ability to achieve high in-plane Q provided that the mode is suitably positioned within the bandgap, and that a sufficient number of periods of the photonic lattice are used (it is still important not to entirely neglect in-plane considerations in cavity designs as the mode volume can be affected significantly). To address vertical radiation losses, the defect geometry can be tailored to reduce couplings to the light cone, even though $\widetilde{\Delta\eta}(\mathbf{k}_\perp)$ does not necessarily have the automatic zeros it had in the case of the square lattice. Examining such tailorings is the focus of this section.

Our first goal is to reduce couplings between the dominant Fourier components of the $\mathbf{H}_{A_2}^{a,a1}$ mode and the light cone. As was demonstrated above for the square lattice, this can be accomplished

Table 2.9: FDTD simulation results for graded hexagonal lattice geometries (images are for the first PC cavity listed below; $d/a=0.75$ in all designs).

Lattice		$ \mathbf{H} $		$ \widetilde{\mathbf{E}}_x $		$ \widetilde{\mathbf{E}}_y $	
							
$(\mathbf{r}/\mathbf{a})_c$	$(\mathbf{r}/\mathbf{a})_{nn}$	$(\mathbf{r}/\mathbf{a})_e$	ω_n	Q_{\parallel}	Q_{\perp}	Q_{tot}	$V_{eff}((\lambda/n)^3)$
0.36	0.325	0.225	0.250	400,000	180,000	123,000	2.41
0.40	0.380	0.30	0.271	1,540,000	76,000	72,000	1.67
0.36	0.355	0.225	0.252	800,000	107,000	94,000	1.18

through a grade in the hole radii as a function of distance from the center of the cavity. In this case, we reduce the hole radius as we move outwards from the central defect. An example of a graded lattice defect design is given in table 2.9, where only the central region of the cavity is shown to help the reader visualize the hole radii grading (the actual cavity used in FDTD simulations has 10 periods of the hexagonal lattice in each direction). The design consists of two levels of confinement. The first level of confinement has a centrally enlarged air hole ($(r/a)_c = 0.35$) followed by a relatively large decrease in hole radius ($(r/a)_{nn} = 0.325$) for the nearest neighbor holes. The hole radii are then parabolically decreased in moving radially outwards (down to $(r/a)_e = 0.225$ at the edge of the crystal), forming the second level of confinement. The effect this has on $\widetilde{\Delta\eta}(\mathbf{k}_{\perp})$ is evident in fig. 2.8(a)-(b), where we plot this function for the single enlarged hole design of the previous section and for the graded lattice design just described. It is clear that $\widetilde{\Delta\eta}(\mathbf{k}_{\perp})$ has been dramatically reduced at $\pm\{\mathbf{k}_{J_1}, \mathbf{k}_{J_3}, \mathbf{k}_{J_5}\}$, limiting the coupling between the dominant Fourier components and the light cone. The magnetic field amplitude and the Fourier transform of the mode's in-plane electric field components are shown in table 2.9. The resulting Q values and mode volume, as listed in table 2.9, are $Q_{\perp} = 1.8 \times 10^5$, $Q_{\parallel} = 4 \times 10^5$, and $V_{eff} = 2.41(\lambda/n)^3$. As previously mentioned, Q_{\parallel} could be made larger by simply increasing the number of periods in the photonic lattice; however, this will not have an appreciable effect on the mode volume, which is somewhat large in this case.

Having achieved a design with a high Q_{\perp} , we would like to modify it so as to reduce the mode

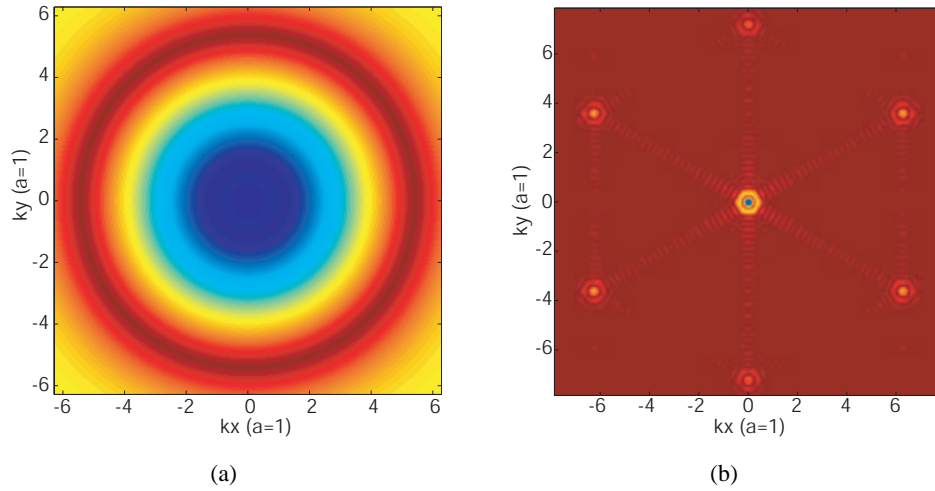


Figure 2.8: (a) $\widetilde{\Delta\eta}(\mathbf{k}_\perp)$ for single enlarged hole design in hexagonal lattice ($r/a = 0.30$, $r'/a = 0.45$). (b) $\widetilde{\Delta\eta}(\mathbf{k}_\perp)$ for graded hexagonal lattice design shown in table 2.9.

volume, which, at $V_{\text{eff}} = 2.41(\lambda/n)^3$, is roughly twice that which we had for square lattice designs. We employ two different modifications to do so; an increase in the average hole radius and a faster grade in the hole radii (the grading occurs over a smaller number of periods than in the first example), both of which should improve in-plane confinement. The results of these modifications are given in the second row of table 2.9; as expected, the in-plane Q has increased considerably, to a value of $Q_{\parallel} = 1.54 \times 10^6$, and the mode volume has decreased to $V_{\text{eff}} = 1.67(\lambda/n)^3$, but at the expense of a decreased vertical Q , now at $Q_{\perp} = 76,000$. The decreased Q_{\perp} is the result of a number of factors. The improved in-plane localization widens the mode in Fourier space, broadening the dominant Fourier components to the extent that they extend into the cladding light cone. The modified grade also changes the magnitude of $\widetilde{\Delta\eta}(\mathbf{k}_\perp)$ at $\pm\{\mathbf{k}_{J_1}, \mathbf{k}_{J_3}, \mathbf{k}_{J_5}\}$, increasing the amount of coupling between the mode's dominant Fourier components and the light cone. In addition, the increase in modal frequency correspondingly increases the radius of the cladding light cone.

As a final example, we consider adjusting the first level of confinement to reduce the mode volume. Starting with our original graded cavity design (the first design of table 2.9), the size of the holes adjacent to the central defect are increased to a value of $(r/a)_{nm} = 0.355$. The results are for the most part intermediate to the first two examples, with $Q_{\parallel} = 8 \times 10^5$ and $Q_{\perp} = 1.07 \times 10^5$. One important exception is that $V_{\text{eff}} = 1.17(\lambda/n)^3$ is actually much smaller than both of the original designs. Upon further consideration, this result is not too surprising; the smaller mode volume and

the relatively large Q_{\perp} are a result of the stronger yet more extended central perturbation to the photonic lattice.

2.7 Defect modes in a compressed hexagonal lattice

Although we have thus far focused on two regular photonic lattices, there are certainly a number of other lattices and structures that are of potential interest. In this section, we consider the use of a compressed hexagonal lattice. The lattice compression introduces additional degeneracies amongst the satellite extrema of the bandstructure, thus providing an additional level of design flexibility that in this case, allows us to efficiently localize defect modes both vertically and in the plane of the dielectric slab.

The defect modes of the previous section were centered about an air hole; for other applications, such as lasers, it may be of interest to have designs centered about a dielectric region, where strong overlap of the optical field with the semiconductor is desirable. Such a mode would be centered about the b -point in fig. 2.2(a). From the standpoint of designing a high- Q mode, the donor and acceptor modes formed at this point do not meet our symmetry criteria, as the dominant Fourier components of the modes (as listed in tables 2.1 and 2.2) are not orthogonal to the available mirror planes (σ_x and σ_y for the C_{2v} symmetry found at the b -point). This is a reflection of the fact that the \mathbf{k}_{X_i} are not mutually orthogonal (nor are the \mathbf{k}_{J_i}). Thus, our motivation behind distorting the photonic lattice is to modify the dominant Fourier components of the defect modes, with the potential of creating a mode, centered about the dielectric, whose properties are in accordance with our momentum space design rules.

2.7.1 Preliminary analysis

We would like to create a mode whose dominant Fourier components are orthogonal to σ_x and σ_y . Such a mode would have dominant Fourier components $\pm\mathbf{k}_{X_1}$ and/or $\pm\mathbf{k}_{J_2}$. Let us begin by considering acceptor modes. By compressing the lattice in the \hat{y} -direction, so that the spacing between two adjacent rows of holes is less than its usual value (changing it from $a\sqrt{3}/2$ to $\gamma a\sqrt{3}/2$, where γ is the compression factor), we intuitively expect the position of the band edges in that direction of Fourier space (corresponding to $\pm\mathbf{k}_{X_1}$) to increase in frequency, perhaps to the point where the valence band edge at X_1 is nearly degenerate with the valence band edge at the J -points. Of course, this qualitative justification leaves many questions unanswered (such as the position of

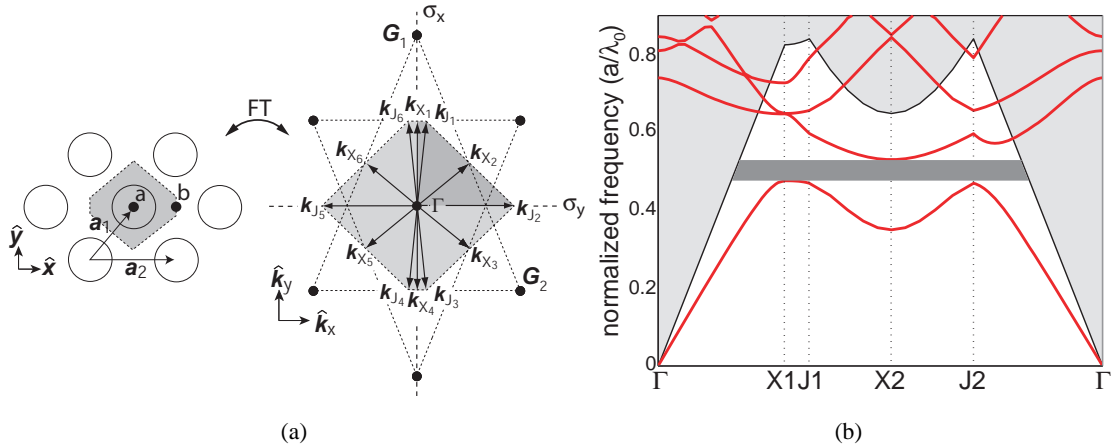


Figure 2.9: (a) Real and reciprocal space lattices of a compressed 2D hexagonal lattice. Refer to table 2.10 for more identification of key geometrical quantities; (b) fundamental TE-like (even) guided mode bandstructure for a compressed hexagonal lattice, calculated using a 2D plane-wave expansion method with an effective index for the vertical guiding; $r/a = 0.35$, $n_{\text{slab}} = n_{\text{eff}} = 2.65$, $\gamma = 0.7$.

the band edges at the other high symmetry points in the lattice). To properly answer these questions, we formulate a symmetry analysis of defect modes in compressed hexagonal lattices, using the methods of chapter 1.

Consider the real and reciprocal space representations of the compressed hexagonal lattice as illustrated in fig. 2.9(a). Compression has reduced the point group symmetry of the lattice to C_{2v} , and the irreducible Brillouin zone (IrBZ) is no longer a $30^\circ - 60^\circ - 90^\circ$ triangle, but is now a quadrilateral, traced between $\Gamma - X_1 - J_1 - X_2 - J_2 - \Gamma$. The modifications in various geometrical quantities associated with the real and reciprocal space compressed lattice are given in table 2.10. Note that, in particular, the group of the wavevector $G_{\mathbf{k}}$ at the X and J points has been reduced in symmetry, and that $|\mathbf{k}_{X_1}| \neq |\mathbf{k}_{X_2}|$ (the \mathbf{k}_{J_i} are still equal in magnitude). Furthermore, $|\mathbf{k}_{X_1}|$ now approaches $|\mathbf{k}_J|$. Indeed, for a compression factor $\gamma = 1/\sqrt{3}$, the vectors coincide and the resulting lattice is in fact square. For compression factors between 0.8 and $1/\sqrt{3}$, the vectors are still quite close in magnitude, and we qualitatively expect that the lowest frequency band (the valence band) will be very nearly degenerate at the X_1 and J points. It is in this way that the compressed hexagonal lattices considered in this section are intermediate to the hexagonal and square lattices. In using the compressed hexagonal lattice we hope to take advantage of the large in-plane bandgap of the hexagonal lattice and the favorable symmetry of the square lattice.

Table 2.10: Key geometrical quantities associated with the standard and compressed hexagonal lattices.

Crystal Parameter(s)	Hexagonal Lattice	Compressed Hexagonal Lattice
G_a^a	C_{6v}	C_{2v}
G_b^b	C_{2v}	C_{2v}
$\{\mathbf{a}_1, \mathbf{a}_2\}$	$\{(\frac{a}{2}, \frac{a\sqrt{3}}{2}), (a, 0)\}$	$\{(\frac{a}{2}, \frac{a\sqrt{3}\gamma}{2}), (a, 0)\}$
$\{\mathbf{G}_1, \mathbf{G}_2\}$	$\{(0, \frac{4\pi}{a\sqrt{3}}), (\frac{2\pi}{a}, -\frac{2\pi}{a\sqrt{3}})\}$	$\{(0, \frac{4\pi}{a\sqrt{3}\gamma}), (\frac{2\pi}{a}, -\frac{2\pi}{a\sqrt{3}\gamma})\}$
$\pm X_1$	$(0, \pm \frac{2\pi}{a\sqrt{3}})$	$(0, \pm \frac{2\pi}{a\sqrt{3}\gamma})$
$\pm X_2$	$(\pm \frac{\pi}{a}, \pm \frac{\pi}{a\sqrt{3}})$	$(\pm \frac{\pi}{a}, \pm \frac{\pi}{a\sqrt{3}\gamma})$
$\pm X_3$	$(\pm \frac{\pi}{a}, \mp \frac{\pi}{a\sqrt{3}})$	$(\pm \frac{\pi}{a}, \mp \frac{\pi}{a\sqrt{3}\gamma})$
$\pm J_1$	$(\pm \frac{2\pi}{3a}, \pm \frac{2\pi}{a\sqrt{3}})$	$(\pm \frac{\pi}{a}(1 - \frac{1}{3\gamma^2}), \pm \frac{2\pi}{a\sqrt{3}\gamma})$
$\pm J_2$	$(\pm \frac{4\pi}{3a}, 0)$	$(\pm \frac{\pi}{a}(1 + \frac{1}{3\gamma^2}), 0)$
$\pm J_3$	$(\pm \frac{2\pi}{3a}, \mp \frac{2\pi}{a\sqrt{3}})$	$(\pm \frac{\pi}{a}(1 - \frac{1}{3\gamma^2}), \mp \frac{2\pi}{a\sqrt{3}\gamma})$
$G_{0, \mathbf{k}_{X_i}}^c$	C_{2v}	C_{2v}
$G_{0, \mathbf{k}_{J_1}}$	C_{3v}	$C_{1v} = \{e, \sigma_y\}$
$G_{0, \mathbf{k}_{J_2}}$	C_{3v}	$C_1 = \{e\}$
$G_{0, \mathbf{k}_{J_3}}$	C_{3v}	$C_{1v} = \{e, \sigma_y\}$

^a Point Group for defect at point a of lattice.

^b Point Group for defect at point b of lattice.

^c Group of the wavevector.

Using the 2D plane wave expansion method with an effective index to account for vertical waveguiding, we arrive at the bandstructure shown in fig. 2.9(b). The compression ratio (γ) has been set at a value of 0.7 for this calculation. We see that the valence band is nearly degenerate at points X_1 , J_1 , and J_2 , and thus, we expect an acceptor mode to be formed by mixing the valence band modes formed at all of these points in Fourier space. Following the symmetry analysis techniques described in chapter 1, we determine approximate forms for valence band modes at these points. Grouping all of them together, we arrive at the following expressions for modes formed about the high symmetry point a shown in fig. 2.9(a):

$$VB_a = \hat{z} \begin{pmatrix} \cos(\mathbf{k}_{X_1} \cdot \mathbf{r}_\perp^a) \\ e^{-i\mathbf{k}_{J_1} \cdot \mathbf{r}_\perp^a} + e^{-i\mathbf{k}_{J_3} \cdot \mathbf{r}_\perp^a} \\ e^{-i\mathbf{k}_{J_4} \cdot \mathbf{r}_\perp^a} + e^{-i\mathbf{k}_{J_6} \cdot \mathbf{r}_\perp^a} \\ e^{-i\mathbf{k}_{J_2} \cdot \mathbf{r}_\perp^a} \\ e^{-i\mathbf{k}_{J_5} \cdot \mathbf{r}_\perp^a} \end{pmatrix} \quad (2.7)$$

Note that the valence band modes formed about the high symmetry point b (found by taking $\mathbf{r}_\perp^b = \mathbf{r}_\perp^a - \mathbf{b}$) differ from these only by constant phase factors and hence the modes above can be used for investigations about b as well. Both the a and b points have C_{2v} symmetry, and the representation of the VB_a basis under C_{2v} , labeled $S^{a,a1}$, is given by $S^{a,a1} = 3A_2 \oplus 2B_2$, where A_2 and B_2 label irreducible representations (IRREPs) of C_{2v} . In our previous analysis, we were able to take such a representation and use projection operators on the basis functions to get approximate forms for the localized modes. In this case, we have no such luxury, as there is no way to distinguish between the modes of the different A_2 (or B_2) subspaces without some additional physical knowledge of the system. The best we can do is to form one projection operator for a composite A_2 subspace and another for a composite B_2 subspace. Doing so yields the following matrices, where the rows and columns are ordered in accordance with that which was chosen for the VB_a modes above:

$$P_{A_2} = \begin{pmatrix} 2 & 0 & 0 & 0 & 0 \\ 0 & 1 & 1 & 0 & 0 \\ 0 & 1 & 1 & 0 & 0 \\ 0 & 0 & 0 & 1 & 1 \\ 0 & 0 & 0 & 1 & 1 \end{pmatrix}, \quad P_{B_2} = \begin{pmatrix} 0 & 0 & 0 & 0 & 0 \\ 0 & 1 & -1 & 0 & 0 \\ 0 & -1 & 1 & 0 & 0 \\ 0 & 0 & 0 & 1 & -1 \\ 0 & 0 & 0 & -1 & 1 \end{pmatrix}. \quad (2.8)$$

By the form of these projection matrices, it is clear that the A_2 modes can potentially be formed from any of the degenerate band edge points $\{\pm\mathbf{k}_{X_1}, \pm\mathbf{k}_{J_1}, \pm\mathbf{k}_{J_2}, \pm\mathbf{k}_{J_3}\}$, while the B_2 modes do not include $\pm\mathbf{k}_{X_1}$. It is our hope to design defects that produce A_2 modes which only contain $\pm\mathbf{k}_{X_1}$ and $\pm\mathbf{k}_{J_2}$, to satisfy our symmetry criteria from section 2.2. To see if this can be the case, in the next section we consider FDTD simulations of defect cavities in this lattice.

Before moving on to discuss FDTD simulations, for the sake of completeness, let us briefly consider donor modes in this lattice. Such modes will be formed from the conduction band edge

located at point X_2 in fig. 2.9(b). Using a symmetry analysis similar to that described above, we determine the conduction band modes for the a and b high symmetry points:

$$CB_a = \hat{z} \begin{pmatrix} \sin(\mathbf{k}_{X_2} \cdot \mathbf{r}_\perp^a) \\ \sin(\mathbf{k}_{X_3} \cdot \mathbf{r}_\perp^a) \end{pmatrix}, \quad CB_b = \hat{z} \begin{pmatrix} \cos(\mathbf{k}_{X_2} \cdot \mathbf{r}_\perp^b) \\ \cos(\mathbf{k}_{X_3} \cdot \mathbf{r}_\perp^b) \end{pmatrix}, \quad (2.9)$$

where $\mathbf{r}_\perp^b = \mathbf{r}_\perp^a - \mathbf{b}$.

The representation of the CB_a basis under C_{2v} (the defect symmetry), labeled $S^{a,d1}$, is given by $S^{a,d1} = B_1 \oplus B_2$, while the representation of the CB_b basis under C_{2v} , labeled $S^{b,d1}$ is given by $S^{b,d1} = A_1 \oplus A_2$. Projecting the CB_a and CB_b bases onto the irreducible representations above, we get

$$\begin{aligned} \mathbf{H}_{B_1}^{a,d1} &= \hat{z} \begin{pmatrix} \sin(\mathbf{k}_{X_2} \cdot \mathbf{r}_\perp^a) - \sin(\mathbf{k}_{X_3} \cdot \mathbf{r}_\perp^a) \\ \sin(\mathbf{k}_{X_2} \cdot \mathbf{r}_\perp^a) + \sin(\mathbf{k}_{X_3} \cdot \mathbf{r}_\perp^a) \end{pmatrix}, \\ \mathbf{H}_{B_2}^{a,d1} &= \hat{z} \begin{pmatrix} \sin(\mathbf{k}_{X_2} \cdot \mathbf{r}_\perp^a) + \sin(\mathbf{k}_{X_3} \cdot \mathbf{r}_\perp^a) \\ \sin(\mathbf{k}_{X_2} \cdot \mathbf{r}_\perp^a) - \sin(\mathbf{k}_{X_3} \cdot \mathbf{r}_\perp^a) \end{pmatrix}, \\ \mathbf{H}_{A_1}^{b,d1} &= \hat{z} \begin{pmatrix} \cos(\mathbf{k}_{X_2} \cdot \mathbf{r}_\perp^b) - \cos(\mathbf{k}_{X_3} \cdot \mathbf{r}_\perp^b) \\ \cos(\mathbf{k}_{X_2} \cdot \mathbf{r}_\perp^b) + \cos(\mathbf{k}_{X_3} \cdot \mathbf{r}_\perp^b) \end{pmatrix}, \\ \mathbf{H}_{A_2}^{b,d1} &= \hat{z} \begin{pmatrix} \cos(\mathbf{k}_{X_2} \cdot \mathbf{r}_\perp^b) + \cos(\mathbf{k}_{X_3} \cdot \mathbf{r}_\perp^b) \\ \cos(\mathbf{k}_{X_2} \cdot \mathbf{r}_\perp^b) - \cos(\mathbf{k}_{X_3} \cdot \mathbf{r}_\perp^b) \end{pmatrix}, \end{aligned} \quad (2.10)$$

as approximate forms for the donor modes at points a and b .

2.7.2 FDTD results

As discussed in the previous sections, we are interested in forming an A_2 symmetry mode in the compressed hexagonal lattice, centered about the b -point, whose dominant Fourier components are situated at $\{\pm\mathbf{k}_{X_1}, \pm\mathbf{k}_{J_2}\}$, to be consistent with the symmetry criterion we have prescribed. The group theory analysis just presented has indicated that the modes of the correct symmetry are acceptor-type modes, and have $\{\pm\mathbf{k}_{X_1}, \pm\mathbf{k}_{J_1}, \pm\mathbf{k}_{J_2}, \pm\mathbf{k}_{J_3}\}$ as their potential dominant Fourier components. We thus begin our FDTD design in the compressed hexagonal lattice by analyzing the dominant Fourier components produced by a simple defect geometry.

Consider the defect geometry depicted in fig. 2.10(a), consisting of four enlarged holes surrounding the b -point in a compressed hexagonal lattice with compression factor $\gamma = 0.7$. FDTD simulations of such a design (choosing, for example, $r/a = 0.30$ and $r'/a = 0.35$), give the mag-

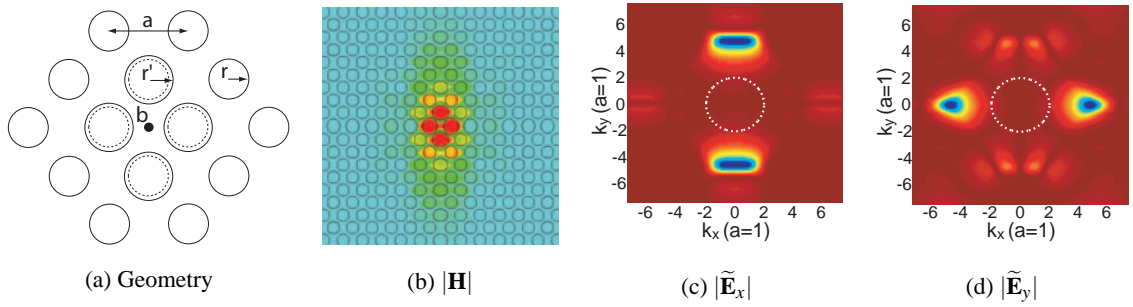


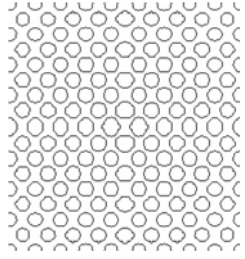
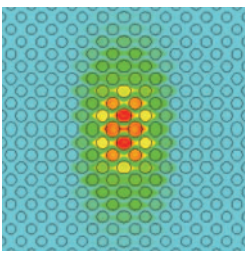
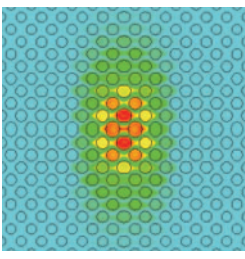
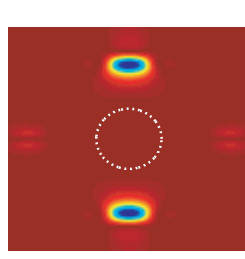
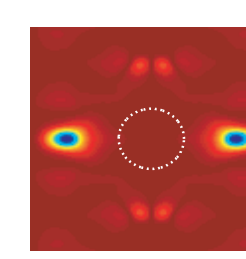
Figure 2.10: Modal characteristics of a simple defect mode in a compressed hexagonal lattice ($d/a = 0.75$).

netic field amplitude and Fourier transformed dominant electric field components shown in fig. 2.10(b)-(d). We see that our defect geometry has produced a mode with dominant Fourier components centered at $\{\pm\mathbf{k}_{X_1}, \pm\mathbf{k}_{J_2}\}$, as desired. Having produced a mode consistent with our symmetry criterion, our next step is to tailor the defect geometry so as to produce a high- Q mode.

The procedure followed is the same as what has been done in the square and hexagonal lattices, namely, we modify the lattice (and therefore $\widetilde{\Delta\eta}(\mathbf{k}_\perp)$) to reduce couplings between the mode's dominant Fourier components (in this case, $\{\pm\mathbf{k}_{X_1}, \pm\mathbf{k}_{J_2}\}$) and the light cone. We do so by starting with a defect consisting of the four enlarged holes surrounding the b -point (we choose $r'/a = (r/a)_c = 0.30$), and then parabolically decreasing the hole radius as we move away from the defect center (down to a value of $(r/a)_e = 0.225$ at the edge of the crystal). The resulting lattice is shown in table 2.11 (only the central region has been shown; in total there are 10 periods of air holes in \hat{x} and 8 periods in \hat{y} surrounding the defect center), along with the magnetic field amplitude and Fourier transformed electric field components for the defect mode. FDTD calculations predict $Q_\perp = 1.5 \times 10^5$, $Q_\parallel = 7.5 \times 10^5$, $Q_{tot} = 1.3 \times 10^5$, and $V_{\text{eff}} = 1.7(\lambda/n)^3$ for this design.

The modifications to the lattice have largely accomplished our objectives, as we have simultaneously achieved high vertical and in-plane Q s, while keeping the modal volume reasonably small (although this value is still larger than our previous designs). Improvements can still be made; for example, simulation results indicate that there are still momentum components present within the light cone of $\widetilde{\mathbf{E}}_y$; hence a further tailoring of the lattice in the \hat{x} -direction ($\widetilde{\mathbf{E}}_y$ has its dominant Fourier components along $\pm\mathbf{k}_{J_2}$) should help increase Q_\perp , though potentially at the expense of a larger mode volume.

Table 2.11: FDTD simulation results for graded compressed hexagonal lattice geometries.

Lattice		$ \mathbf{H} $	$ \tilde{\mathbf{E}}_x $	$ \tilde{\mathbf{E}}_y $		
						
$(\mathbf{r}/\mathbf{a})_c$	$(\mathbf{r}/\mathbf{a})_e$	ω_n	Q_{\parallel}	Q_{\perp}	Q_{tot}	$\mathbf{V}_{\text{eff}}((\lambda/n)^3)$
0.30	0.225	0.323	755,000	152,000	127,000	1.72

2.8 Summary

The design of high- Q defect modes in a 2D PC slab WG has been developed through use of momentum space methods. Starting with the fundamental criterion that the reduction of vertical radiation losses requires an elimination of momentum components within the light cone of the slab waveguide, we proceed to present methods by which this is accomplished. The first is through a judicious choice of the mode's symmetry so that it is odd about mirror planes orthogonal to the mode's dominant Fourier components. To determine the precise nature of the symmetry for such modes in square and hexagonal lattices, we refer to the symmetry analysis of chapter 1, from which we produce a set of candidate modes that satisfy this momentum space criterion. Although symmetry alone can reduce vertical radiation loss, further modifications of the defect geometry based upon Fourier space considerations can be used to increase Q even further. Tailoring the lattice to avoid momentum space couplings which lead to in-plane and vertical radiation losses, we present graded square lattice structures for which Q_{\perp} exceeds 10^5 while maintaining Q_{\parallel} in the $3\text{-}5 \times 10^5$ range, demonstrating the possibility of producing high- Q modes in a planar PC slab WG by using these techniques. Similarly, we have used these techniques to produce cavity geometries within the regular and compressed hexagonal lattices that have total Q s in excess of 10^5 . The ability to create high- Q cavity geometries in three different lattices is an indication of the generality of this Fourier space-based approach.

As I have mentioned in the preface, after our contributions to the area of high- Q cavity design [21, 23], a number of groups have continued this work and have succeeded in developing designs

with predicted Q factors in excess of 10^6 [26, 27, 28, 29, 30]. Momentum space design principles remain the basis for most of these works, and in particular, the analysis of the spatial Fourier transform of the cavity mode field patterns has more or less become a standard approach in PC cavity design. The physical intuition behind the adoption of different cavity geometries is often thought of in different ways. The picture that we have followed is one that involves an examination of modal couplings in Fourier space, where the dielectric perturbation that forms the defect (or more precisely, its Fourier transform) is the key quantity that should be tailored to avoid the creation of modes that contain leaky Fourier components, where such problematic regions of Fourier space are well known to be the cladding light cone (for vertical radiation loss) and the range of angles and momenta for which the photonic lattice is not highly reflective (for in-plane losses). As a slightly different take on this, one can consider what the field profile of such a ‘good’ mode (i.e., one that does not contain small momentum components) looks like in real space, and then consider how to tailor the a given defect geometry to achieve this. This is essentially the approach taken in ref. [51]. More recently, some authors [28, 30] have used a PC waveguide mode as the starting point for creating PC cavities; that is, the cavity is formed through some localized modification to the geometry of a PC waveguide. This has been done by both changing the lattice constant within some region of the waveguide [28] and by shifting the position of some small number of holes within the structure [30]. Although there a number of different ways in which one can view these designs, a simple way to think about this is that a PC waveguide mode has the advantage of having a well-defined in-plane momentum along the waveguide (its propagation constant) which lies outside of the cladding light cone. It thus makes intuitive sense that there is a benefit to starting the cavity design with such a mode that, in principle, is free of radiation losses. As a side comment, this class of design is actually not that far astray from the graded square lattice cavity design presented in this chapter. The PCWG designed in ref. [33] is based upon our square lattice cavity design, where the grade in hole radius along the \hat{x} -axis is essentially kept, but the structure is not graded along the \hat{y} -axis (it has translational periodicity in this dimension). One could imagine creating a cavity that consists of a short section of this PCWG sandwiched between a pair of appropriately designed DBR mirrors that could, for example, be PCWGs with a different lattice constant or grade in hole radius. Such a design would, in principle, be very similar to those of refs. [28, 30]. This is actually relatively close to what has already been done, where the end mirrors can be thought of as the uniform PC lattice surrounding the graded section. The key to additional improvements would be to further tailor the geometry to better avoid radiation losses. At some level, this becomes somewhat difficult to do within the square

lattice because of the small in-plane bandgap, which means that in-plane losses can not be neglected (they often can be within the hexagonal lattice). In addition, it should be noted that the cavity design procedure adopted in this chapter is in part based on the utilization of modes of odd spatial symmetry in order to reduce vertical radiation losses, and as further described in chapter 4, to create a cavity design that is relatively robust to fabrication-induced imperfections. These restrictions could potentially be relaxed in future designs, in favor of other mechanisms for accomplishing the same goals. In particular, as the ability to precisely reproduce designs in fabricated structures improves, the necessity for a robust cavity design is reduced.

The momentum space analysis described in this chapter essentially tells us which portions of Fourier space to avoid to create high- Q structures; one might then expect that this could be used as the input to some type of automated computational technique that would generate the field patterns, and the associated dielectric functions, for modes that satisfy the criteria. Additional constraints on the mode volume and the robustness of the cavity geometry to imperfections, for example, could be added to such an analysis. Initial attempts to incorporate at least some amount of this inverse design approach, along with optimization methods for determining the highest possible Q and associated dielectric function within some region of parameter space, have been reported in refs. [31, 29]. Such approaches have a lot of merit in that they can eliminate the trial-and-error approach that is often used to design high- Q structures. This is particularly important in the design of these PC cavities, as FDTD simulations are often computationally intensive (a 3D simulation of the cavity field and the determination of its quality factor often takes one day of computing time on our Pentium III machines). However, one has to be mindful of the large parameter space over which such optimization techniques must, in principle, operate. At the most complex level, one can imagine that the only constraint on the physical structure is that the dielectric function at every grid point in the simulation can only be one of two values (that of the semiconductor material or that of air). Obviously, the simulation can be further constrained to only allow those dielectric functions that are physically realizable (some minimum feature size can be specified). Nevertheless, the number of potential configuration over which an optimization, for example, must be run is still quite considerable. The physical insight gained by techniques such as the group theory and Wannier analysis of chapter 1, as well as the momentum space design of this chapter, is thus very important from the standpoint of further constraining these problems by, for example, specifying the lattice to be considered, the high symmetry point about which a defect is to be formed, or the type of mode (donor or acceptor) to be considered. The specification of the lattice may be dictated by the desire to create modes of a

certain polarization, dominant emission direction, or location of the peak electric field, for example.